Supporting Information

Nelson et al. 10.1073/pnas.1406535111

SI Methods

Determination of Vesicle Size. Vesicles of consistent sizes were prepared by a well-established technique in which rehydrated lipid preparations were extruded through filter membranes with defined pore sizes (1). Vesicle size distributions were measured in a flow cytometer by the method of Vorauer-Uhl et al. (2) using a series of latex bead size standards. The height of the side-scatter signal for these beads was linear with the bead volume (Fig. S1*A*), which, assuming spherical particles, is thus related to the bead diameter. Based on this standard curve, we measured the distribution of vesicle diameters to be within 10% of the pore diameter over the range of 200–650 nm (Fig. S1 *C*–*E*). The 100-nm vesicles were at the sensitivity limits of the equipment, resulting in the relatively large variance in diameter estimates for this preparation (Fig. S1*B*). Throughout this manuscript, we refer to the resulting vesicle diameters according to the filter pore size used (i.e., 100-, 200-, 400-, and 650-nm diameters).

Quantification of Motor:Vesicle Binding. To determine the number of bound motors per vesicle, we used the fluorescence photobleaching approach described by Nayak and Rutenberg (3). We prepared vesicles by mixing an estimated 11.3 nM of 200-nm 1,2-dioleoyl-*sn*-glycero-3-phosphocholine (DOPC) vesicles (see below) with 45.2–362 nM myosin Va (myoVa), representing motor-to-vesicle mixing ratios ranging from 4:1 to 32:1 (the mixing ratios used in the manuscript). Vesicle suspensions were then diluted 50× and added to a flow cell with a bare glass surface and imaged at 10FPS under standard total internal reflection fluorescence (TIRF) conditions (described in *Methods*). Particles landing on the glass surface (within the TIRF field) were identified using a custom-written "rolling subtraction" macro in ImageJ where the pixel intensities in frame (i) are subtracted from those in frame ($i + 5$). The output image stack is then *Z*-projected using the "Maximum" setting, and spots larger than 9 square pixels are identified using the *Analysis → Analyze Particles* function of ImageJ. Finally, for each "region of interest" (ROI) identified as a particle, the integrated image intensities within the original image stack were determined using the "Multimeasure" function of ImageJ and saved as a text file along with the *X*–*Y* coordinates of the ROI. Then, integrated intensities are fit with the following form using least-squares fitting in R (a statistical programming language):

$$I(t) = \begin{cases} I_B, t < L \\ I_B + I_0 e^{-(t-L)/\tau}, t \geq L, \end{cases}$$

where $I(t)$ is the integrated intensity at time t, I_B is the background intensity before vesicle landing (and subsequent to complete photobleaching), I_0 is the integrated intensity upon vesicle landing ($t = L$), and τ is the fluorescence decay rate. Sample fluorescence intensity time courses are shown in Fig. 1*A*. ROIs were omitted from the dataset if they were poorly fit, had extremely rapid decay kinetics ($\tau > 0.05$ frame^{-1}), or low initial intensities, relative to background ($I_0 < 2{*}I_B$). For each condition, 400 candidate particles were collected from 15 1,000-frame (100-s) recordings.

Within each condition, fluorescence intensity variance (σ_I) between photobleaching curves (Fig. 1*B*) were calculated as follows:

$$\sigma_I^2 = \left\langle (I - \langle I \rangle)^2 \right\rangle.$$

The ensemble σ_I^2 vs. photobleached fraction [p, defined as $\exp(-t/\tau)$] is shown in Fig. 1*C*. Subsequently, the intensity per fluorophore (v; shown for each condition in Fig. 1*D*, light bars) is then calculated according to equation 6 in Nayak and Rutenberg by integrating under the curve of σ_I^2 vs. p (Fig. 1*C*):

$$v = 6 \int_0^1 \frac{\sigma_I^2 dp}{I_0}.$$

The number of motor molecules per vesicle (n) is then calculated according to the following:

$$n = 2\frac{I_0}{v},$$

where n is the number of motors, assuming two YFPs per molecule. The resulting estimates of the number of bound motors per vesicle are shown in Fig. 1*E*. This approach shows an approximately linear increase in the number of motor molecules per vesicle, up to 15 motors, with no subsequent increase in motor binding at mixing ratios of 32 motors per vesicle. Larger vesicles were not analyzed using this approach, as there was a prolonged period of increasing fluorescence subsequent to initial vesicle landing, making determination of the initial fluorescence (I_0) problematic. We attribute this to the vesicle diameter (400- and 650-nm vesicles) being larger than the height of the evanescent field (~200 nm). Therefore, upon a vesicle landing on the glass surface, a significant number of YFPs remain outside the illumination, although they are likely able to diffuse in and out of the evanescent field, resulting in a more complex (and not necessarily exponential) fluorescence decay curve.

Estimation of Vesicle Yield. To estimate the total vesicle yield, we used an alternate, bulk approach. We determined the concentration of 1,1′-dioctadecyl-3,3,3′3′-tetramethylindocarbocyanine perchlorate (DiI)-labeled 1-μm vesicles using a standard hemocytometer (Fisher Scientific). Unfortunately, small vesicles diffuse too rapidly in the sample chamber for suitable quantization by this approach. However, as the vesicles in this study were produced by reextruding 1-μm vesicles to the desired size, we used a 1-μm-pore diameter filter in the extruder for both the first and second extrusion steps. In the sample preparation, the final lipid concentration was 4.25 g/L, which predicts a theoretical yield of 575 pM of 1-μm-diameter vesicles (assuming 1×10^7 lipid molecules per 1-μm spherical vesicle). The experimentally observed concentration was 502 ± 149 pM (n = 54 hemocytometer sectors) after the first extrusion step, and 434 ± 204 pM (n = 80 hemocytometer sectors) after the second extrusion step, indicating a yield of 87% for each extrusion step, or a final yield of 75.5% for the entire preparation procedure. Adjusting for the number of lipid molecules per vesicle, this indicates that for 200-nm vesicles, the yield was 11.3 nM vesicles.

Monte Carlo Simulation

We simulate the motion of vesicles through a stepwise, 1D Monte Carlo-style simulation. A flowchart illustrating the steps of the simulation is shown in Fig. S6 with the details of the simulation within each numbered step described below. Rates, parameters, equations, and their sources are detailed in Table S1.

1) Initiate simulation: Each simulation begins with a vesicle of defined radius (R), composition (membrane diffusion constant, D), and number of motors (N), with a single motor bound to the track ($N_{\mathrm{bound}} = 1$). At the start of each simulated trajectory, both the single engaged motor and the vesicle are considered to be at the position $X = 0$ nm. During the simulation, motors exist in one of two states: bound to actin at a unique position (X), or not bound to actin (indicated as no recorded position, or "NA" for a given iteration). In this simulation, each iteration (Δt) represents 1 ms of time. Within each iteration, motors that are not currently bound to the track can bind to the track, whereas each of the track-engaged motors can either step or detach (thus returning to the unbound pool). The probability that a particular event (binding, unbinding, or stepping) occurs during an iteration is determined by a random number generated from a binomial distribution with a probability of success equal to the event's rate multiplied by the iteration time (Δt).
2) MyoVa:actin binding: The rate of an unbound motor binding to actin (k_{bind}), which we calculate using the mathematical description for cell surface receptor:ligand binding (4), depends upon the motor's chemical binding rate (k_{on}). k_{bind} (equation in Table S1) is a function of the motor's diffusion constant within the membrane (D), and an "encounter radius" (s), which determines how close a myoVa molecule needs to be to the actin track to be capable of binding. In our description, the geometry of the vesicle and track impinge upon the steric accessibility (Ac) of individual binding sites on the actin track. Some regions of the track are obstructed by the proximity of the vesicle, whereas others lie too far from the vesicle surface to be bridged by a myoVa molecule. This is described in more detail below (*Geometric Constraints on MyoVa:Actin Binding*) and in Fig. S7. Binding to locations already occupied by another motor (within cutoff distance, c) is also prohibited. Ultimately, the probability of a particular motor binding to a specific location on the track is given by $k_{\mathrm{on}}^{*}\,\Delta t^{*}Ac$.
3) Determine force: Actin-bound motors can either detach from or step along the track. Rates governing both of these processes are force sensitive. We describe intermotor forces (F) using a two-component relationship (shown in Table S1) to describe (*i*) forces parallel to the vesicle membrane, which can be relaxed by sliding the motor:vesicle attachment point, and (*ii*) forces perpendicular to the vesicle surface, which constitute a component that cannot relax by repositioning the motor:vesicle attachment. In our description of these forces, "resistive" forces, i.e., those directed opposite to myoVa's processive movement, are indicated with positive values of F, whereas "assistive" forces are indicated with negative values of F. This force description is explained in more detail below (*Intermotor Forces*) and in Fig. S8.
4) MyoVa stepping: Within each iteration of the simulation, each of the actin-bound motors has an opportunity to step along the track (incrementing X by ΔX_{step} for the given motor). We use the force-sensitive stepping kinetics described by Kad et al. (5) to calculate the probability of a step, which indicates that the stepping rate (k_{step}; equation shown in Table S1) is force sensitive, whereas the step size (ΔX_{step}) of myoVa is force independent and normally distributed at 36 ± 9 nm. If a step is indicated, but would result in a motor bound to the track less than the exclusion distance (c) from another track-engaged motor, that step does not occur and the status and position of the indicated motor are not altered.
5) MyoVa:actin detachment: Similarly, within each iteration, each motor has an opportunity to detach with a probability of $k_{\mathrm{off}}^{*}\,\Delta t$ We use the force sensitivity of myoVa detachment described by Vilfan (6), which indicates that the rate of detachment of myoVa from the actin track (k_{off}) is accelerated with assistive (forward) directed forces (indicated with negative values of force, F), and remains insensitive to resistive forces.
6) Center vesicle over bound motors: The vesicle itself is considered to be a tethered diffusing particle, with its mean position centered between the front- and rear-most motors.
7) At the conclusion of each iteration, the center-of-mass position of each actin-bound motor (X) is recorded in a table. Also recorded at the conclusion of each iteration is the force (F) for each track-engaged motor.
8) Vesicle velocity is determined by linear regression to a plot of the vesicle's position vs. time, but only if a vesicle remains processive for at least 500 iterations. Simulations are terminated after 2,000 iterations (2 s of simulated time). Velocity distributions represent 1,000 independent simulations of a particular experimental condition (vesicle size, motor density, etc.).

Geometric Constraints on MyoVa:Actin Binding. The geometry of the vesicle and track dictate where myoVa motors can bind actin, as portions of the vesicle lie either too far or too close to the track to accommodate a myoVa molecule (Fig. S7*A*). Furthermore, the vesicle undergoes thermal motion, so the geometry is constantly changing, although engagement of additional motors restricts this search space. We developed a simple geometric simulation to explore binding-site accessibility. In this approach, we randomly sample possible vesicle positions, as bounded by the maximal reach of the tethering motor(s) (I). For each vesicle position, the steric accessibility (Ac) of a potential binding site is evaluated according to the following:

$$Ac(x\mid d,L)=\begin{cases}0, d>L\\ d/L, d<L,\end{cases}$$

where d is the distance between the actin and vesicle surface at position x along the actin track, and L is the length of the motor (60 nm). After integrating over possible vesicle positions, the result is an empirical probability function for binding at each position along the actin for a given configuration. However, when two or more motors are bound to the actin, the distance between motors also becomes a parameter (I in Fig. S7*B*), as this spacing constrains the Brownian excursions of the vesicle. For large values of I, vesicle motion is highly constrained, with the central region held too close to accommodate additional motors. Therefore, the binding probability function becomes a 2D function (Fig. S7*C*), depending on both the position along the track (x) and the distance between engaged motors (I).

We also considered three descriptions of the accessibility of actin-binding sites due to the helical nature of the actin filament. Reports including Steffen et al. (7) and Veigel et al. (8) have reported a periodicity in myosin's (both myosin II and myosin Va) utilization of binding sites, matching the 36-nm half-turn of the actin double helix. In the 2D myosin:actin binding probability density shown in Fig. S7*C*, we considered the actin to present a uniform array of available binding sites. This is illustrated by the green line in Fig. S7*D*. The two alternate forms termed "strict" (blue line in Fig. S7*D*), wherein only 18 nm off each 36-nm half-turn are accessible for myosin binding, or "relaxed" where all binding sites have some accessibility, but there remains a periodicity to this accessibility (red line in Fig. S7*D*). The resulting 2D binding probability functions are shown in Fig. S7*E*. Finally, we ran simulations using each of these binding probability functions for 200-nm DOPC vesicles at motor densities ranging from 4 to 32 motors per vesicle. Trends in the resulting "fast" and "slow" vesicle populations are shown in Fig. S7*F*, and indicate that the accessibility of binding sites due to the actin helix only influences the simulation result at the highest motor densities, which are not experimentally achieved due to motor binding saturation at 15 motors per vesicle (Fig. 1*E*).

Intermotor Forces. We define the intermotor forces as the sum of two terms, which relate to two different aspects of the vesicle system: (*i*) "relaxable" force, which refers to the forces tangent to the vesicle membrane ($\theta \sim 0°$, as in Fig. S8*A*) that can be relaxed by "sliding" the motor's attachment point along the vesicle membrane, and (*ii*) forces normal to the vesicle membrane ($\theta \sim 90°$, as in Fig. S7*B*) at the point of attachment that cannot be relaxed through repositioning the motor:vesicle attachment point. Motor steps are the main source of intermotor forces, the relaxable component of which then decays over time. Effectively, individual motor steps create force "spikes" (Fig. 6*B*), which relax over time, effectively within a single 1-ms iteration of the simulation for fluid DOPC membranes. The nonrelaxable component then becomes the endpoint to which these forces asymptotically decay.

In the simulation, the relaxable component is described as a simple "spring-and-dashpot" system according to the following:

$$\frac{k \cdot \Delta X_{\text{step}}}{N_{\text{bound}}} \cdot e^{\frac{-(t-t_{\text{step}})Dk}{k_{\text{B}}T}},$$

where k is the bending stiffness of the myosin, D is the membrane diffusion coefficient, ΔX_{step} is the size of the most recent motor step, t is the time point being simulated, and t_{step} is the time of the most recent motor step.

The nonrelaxable component is driven by the geometry of the vesicle and motor ensemble and includes the axial component of forces that are normal to the vesicle surface:

$$\frac{k \cdot (I/2)^2}{2(L+R)},$$

where k is the bending stiffness of the myosin, I is the spacing of motors along the track, relative to the vesicle center, L is the length of the myosin molecule, and R is the vesicle radius. The contribution of this component as a function of a motor's position relative to the vesicle is indicated by the blue line in Fig. S8*C*.

Resistive loads are indicated as positive values of F, whereas assistive loads are indicated with negative values of F. Following this definition, subsequent to a step by the trailing motor, the vesicle membrane is compressed (Fig. S8*A*), and the lead motor is "pushed" forward (i.e., experiences an assistive load, indicated with negative values of F). However, this configuration relaxes (very rapidly with a DOPC membrane) toward a configuration with lower motor loads, indicating that the intermotor force is dominated by the relaxable component in this configuration. Conversely, subsequent to a step by the leading motor (Fig. S8*B*), tension is generated on the vesicle membrane, and the trailing motor is now "pulled" forward (assistive load, indicated with negative F). However, this tension can no longer be alleviated via repositioning of the motor:vesicle attachment point, indicating that, in this configuration, intermotor forces are dominated by the nonrelaxable component.

In our definition of intermotor forces, all engaged motors experience some amount of external force when there is more than a single engaged motor, even at very low motor separation distances (I). We also considered an alternate definition of the intermotor forces that omits the nonrelaxable component—i.e., forces are able to relax to zero load, except in extreme cases in which motors are at the limits allowed by the vesicle geometry. Due to the extremely rapid relaxation rates on DOPC membranes (effectively complete within the 1-ms time step of the simulation), the force experienced by motors on these fluid vesicles is nearly zero, except at the extreme edges of the vesicle (green curve, Fig. S8*C*). We then simulated vesicle trajectories for DOPC vesicles, ranging from 100 to 650 nm in diameter at a constant motor density (corresponding to eight motors per 200-nm vesicle, as in Fig. 3 *B* and *C* in the main manuscript). The resulting velocities of the fast and slow vesicles are shown in Fig. S8*D*, indicating that, without the nonrelaxable force component, the simulation is unable to recapitulate the experimentally observed increase in velocity of the fast component (red lines, Fig. S8*D*).

1. Saffman PG, Delbrück M (1975) Brownian motion in biological membranes. *Proc Natl Acad Sci USA* 72(8):3111–3113.
2. Ramadurai S, et al. (2009) Lateral diffusion of membrane proteins. *J Am Chem Soc* 131(35):12650–12656.
3. Nayak CR, Rutenberg AD (2011) Quantification of fluorophore copy number from intrinsic fluctuations during fluorescence photobleaching. *Biophys J* 101(9):2284–2293.
4. Lauffenburger DA, Linderman JJ (1993) *Receptors: Models for Binding, Trafficking, and Signaling* (Oxford Univ Press, New York).
5. Kad NM, Trybus KM, Warshaw DM (2008) Load and Pi control flux through the branched kinetic cycle of myosin V. *J Biol Chem* 283(25):17477–17484.
6. Vilfan A (2005) Elastic lever-arm model for myosin V. *Biophys J* 88(6):3792–3805.
7. Steffen W, Smith D, Simmons R, Sleep J (2001) Mapping the actin filament with myosin. *Proc Natl Acad Sci USA* 98(26):14949–14954.
8. Veigel C, Wang F, Bartoo ML, Sellers JR, Molloy JE (2002) The gated gait of the processive molecular motor, myosin V. *Nat Cell Biol* 4(1):59–65.

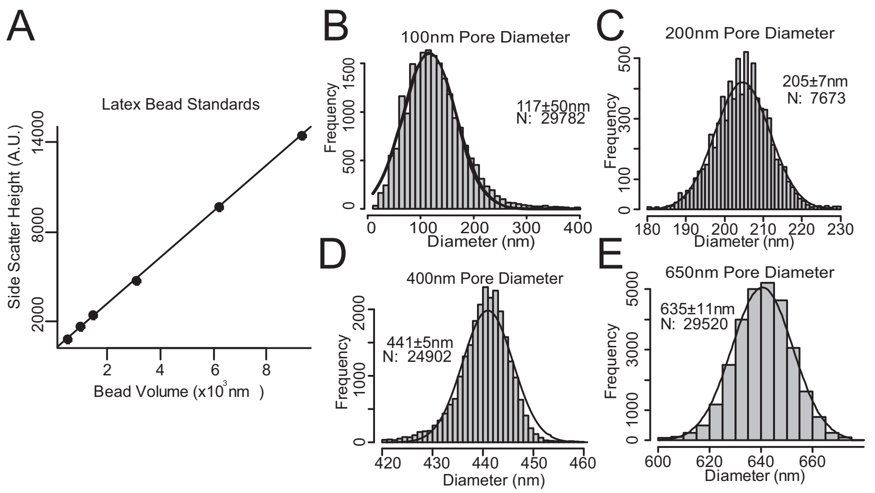

Fig. S1. Vesicle size determination. (*A*) Standard curve constructed using commercially available latex beads demonstrates that side-scatter height (SSH) in a fluorescence cell sorter is linearly related to bead volume. (*B*) Vesicle diameter distributions for vesicles extruded through (*B*) 100-nm, (*C*) 200-nm, (*D*) 400-nm, or (*E*) 650-nm pores. All distributions indicate mean vesicle diameters within 10% of the pore diameter. The wider size distribution seen for smaller vesicles may be partially attributed to very low light-scattering signal and proportionally larger measurement error.

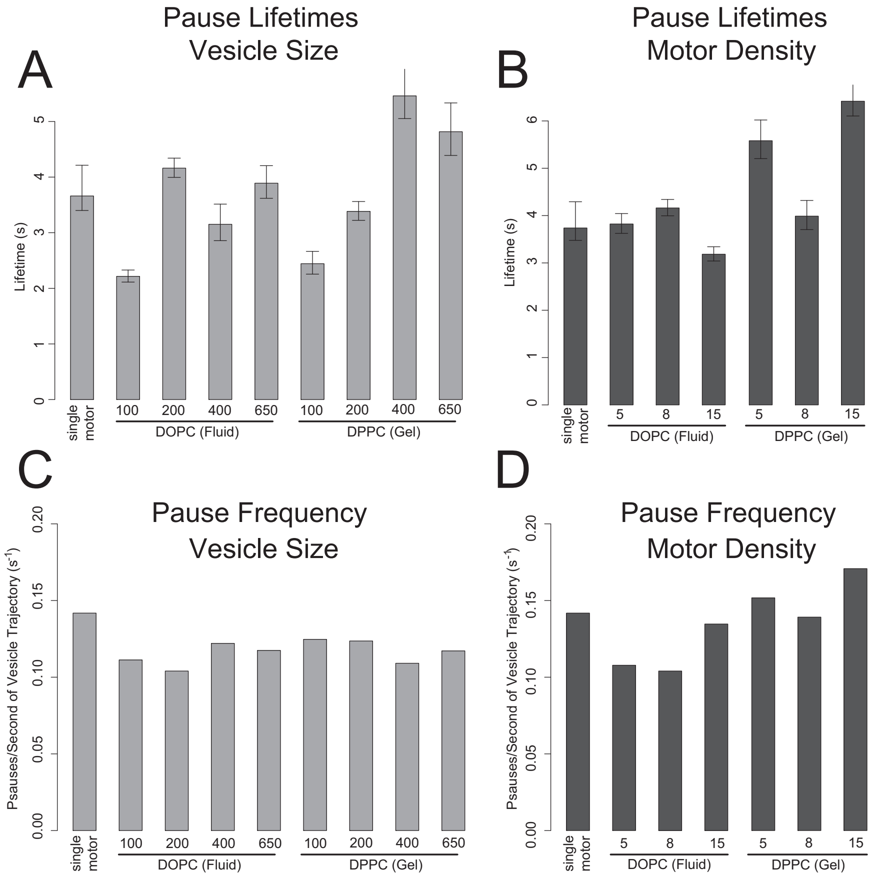

Fig. S2. Pause lifetimes and frequency. Pause lifetimes and frequency as a function of (*A* and *C*) vesicle size, or (*B* and *D*) motor density. Pause frequency is calculated as the total number of pauses divided by the total tracking time for a given condition. Error bars indicate the 95% confidence interval for fitted values.

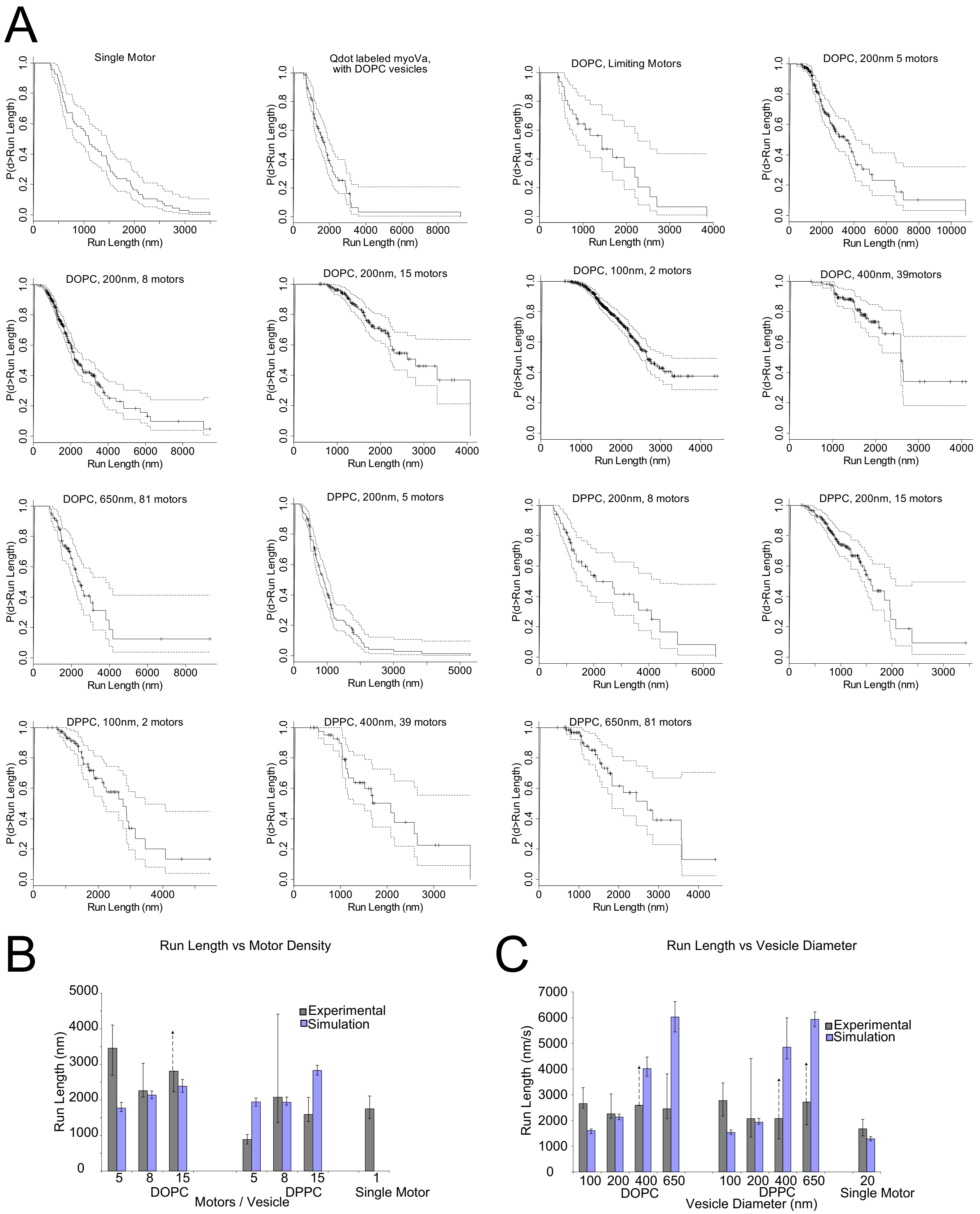

Fig. S3. Run length distributions. (*A*) Run Lengths for single myoVa motors and each vesicle condition are shown as Kaplan–Meier survival plots. Tick marks on the survival curves indicate trajectories that were visually limited by track length, whereas the dashed lines indicate confidence intervals. Comparison of experimental and simulation histograms show median run lengths as a function of (*B*) motor density and (*C*) vesicle diameter. Error bars indicate 95% confidence intervals. "Open intervals," where no upper bound on run length can be determined, are indicated by dashed arrows in place of error bars.

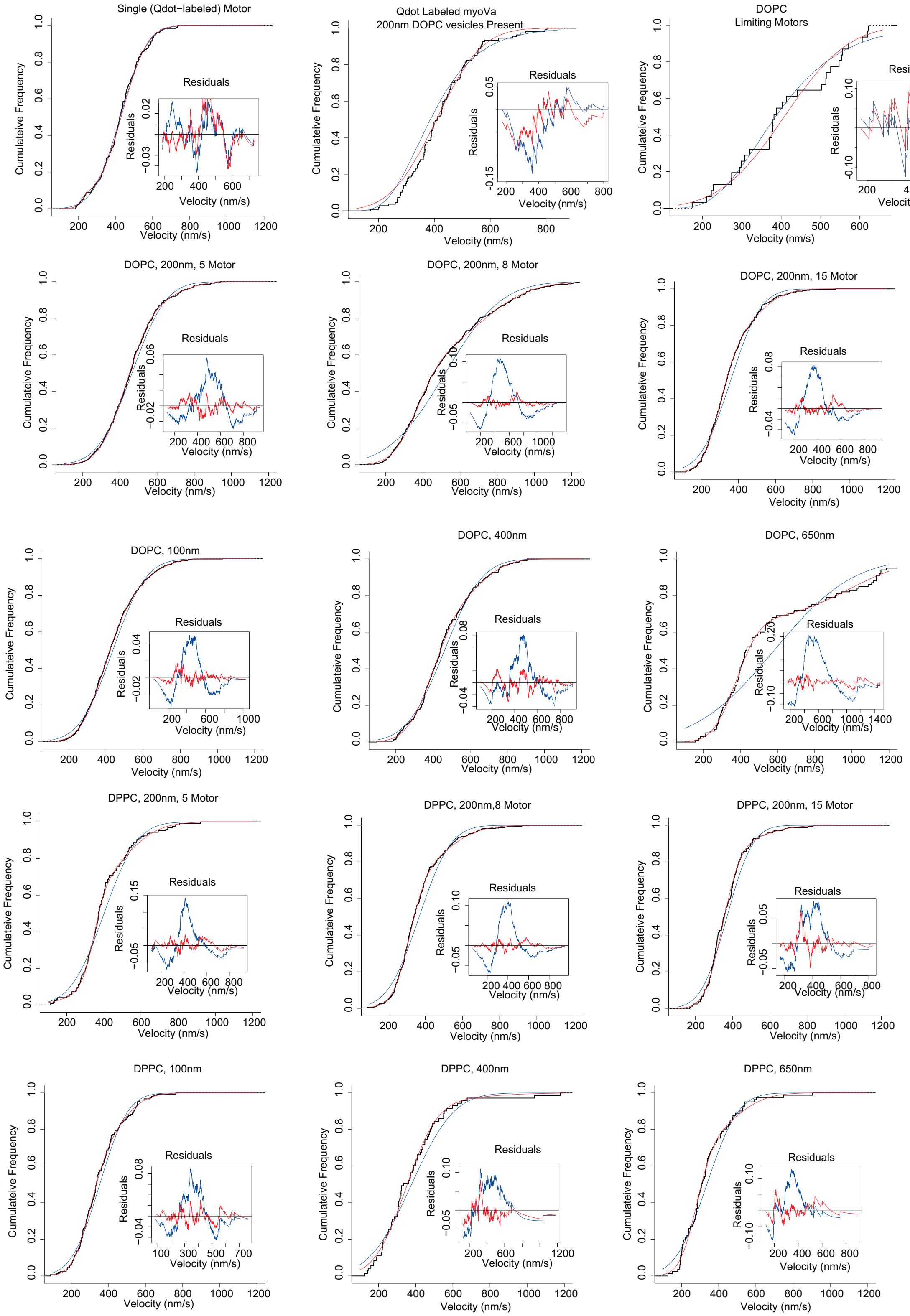

Fig. S4. Cumulative velocity distributions. Velocity distributions for single motors and each vesicle condition, shown along with single (blue)- and double (red)-Gaussian fits. Residuals for each fit are shown in *Insets* and colored accordingly.

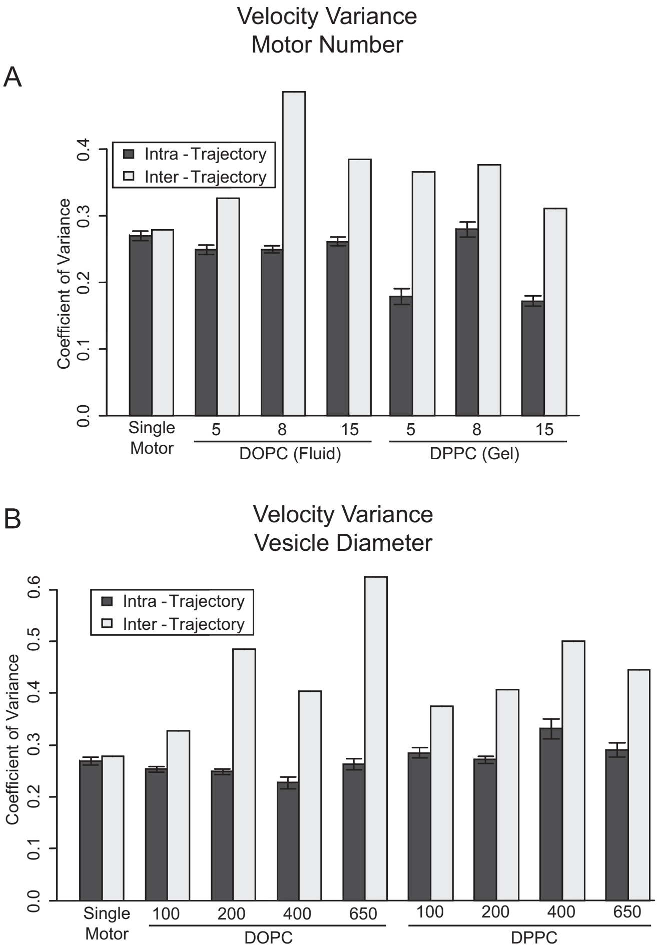

Fig. S5. Intrarun and interrun variance. Coefficient of variance values (defined as the ratio of SD to mean) measuring variance within individual trajectories (dark bars) is lower than variance between trajectories (light bars), regardless of (*A*) motor number or (*B*) vesicle diameter.

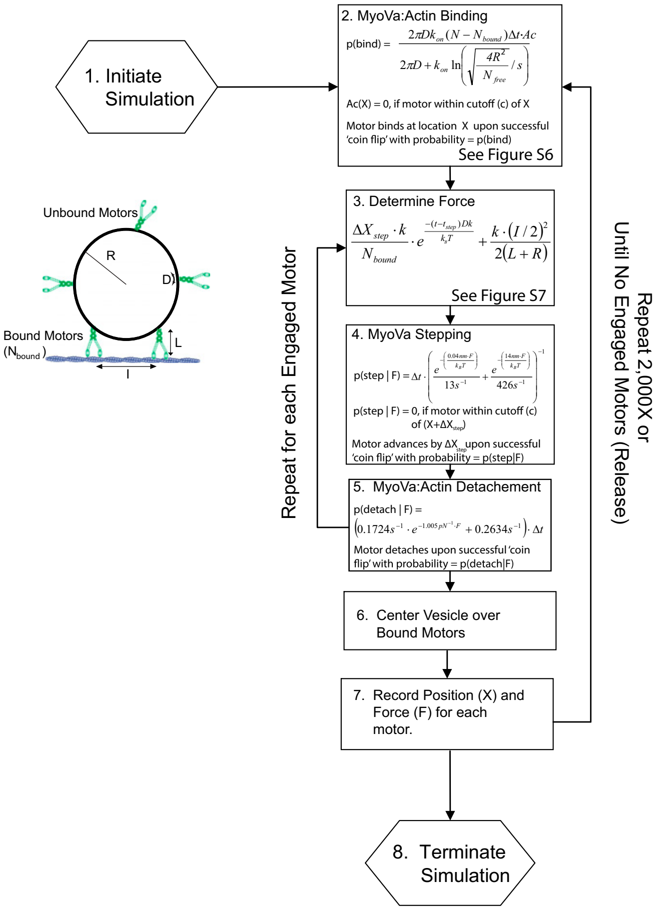
1. Initiate Simulation
2. MyoVa:Actin Binding
$p(\text{bind}) = \frac{2\pi D k_{on}(N - N_{bound})\Delta t \cdot Ac}{2\pi D + k_{on}\ln\left(\sqrt{\frac{4R^2}{N_{free}}}/s\right)}$
Ac(X) = 0, if motor within cutoff (c) of X
Motor binds at location X upon successful 'coin flip' with probability = p(bind)
See Figure S6
3. Determine Force
$\frac{\Delta X_{step} \cdot k}{N_{bound}} \cdot e^{\frac{-(t-t_{step})Dk}{k_B T}} + \frac{k \cdot (I/2)^2}{2(L+R)}$
See Figure S7
4. MyoVa Stepping
$p(\text{step} \mid F) = \Delta t \cdot \left(\frac{e^{-\left(\frac{0.04 nm \cdot F}{k_B T}\right)}}{13 s^{-1}} + \frac{e^{-\left(\frac{14 nm \cdot F}{k_B T}\right)}}{426 s^{-1}} \right)^{-1}$
p(step | F) = 0, if motor within cutoff (c) of ($X+\Delta X_{step}$)
Motor advances by ΔX_{step} upon successful 'coin flip' with probability = p(step|F)
5. MyoVa:Actin Detachement
p(detach | F) =
$\left(0.1724 s^{-1} \cdot e^{-1.005 pN^{-1} \cdot F} + 0.2634 s^{-1}\right) \cdot \Delta t$
Motor detaches upon successful 'coin flip' with probability = p(detach|F)
6. Center Vesicle over Bound Motors
7. Record Position (X) and Force (F) for each motor.
8. Terminate Simulation
Repeat for each Engaged Motor
Repeat 2,000X or Until No Engaged Motors (Release)
Unbound Motors
R
D
Bound Motors (N_{bound})
L
I

Fig. S6. Simulation flowchart. Flowchart illustrating the steps of the Monte Carlo simulation, including illustration of vesicle and geometry-related simulation parameters.

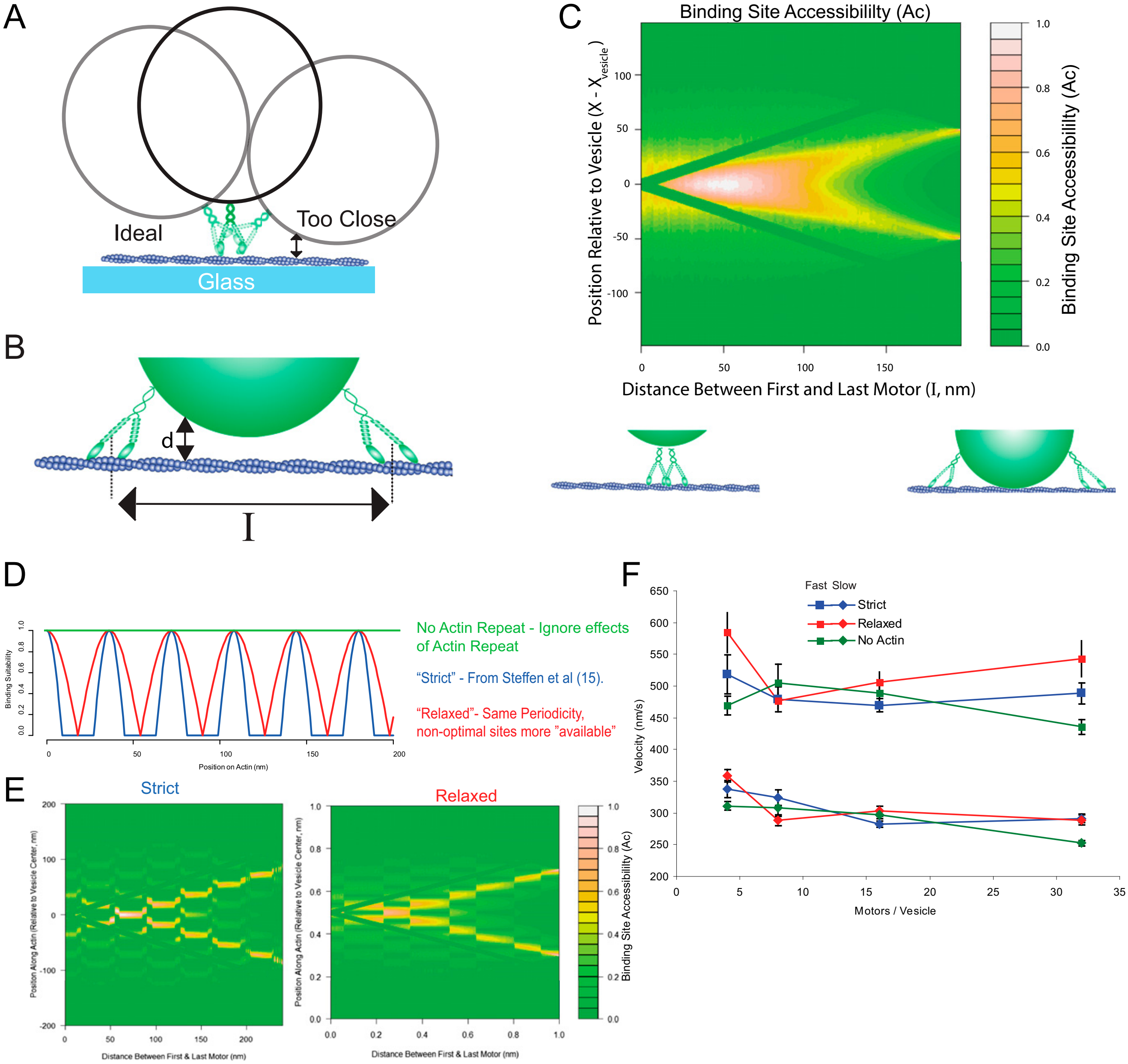

Fig. S7. Geometric constraints of myoVa:actin binding. (*A*) Illustration of diffusing vesicle, tethered by single myoVa. Some configurations have the vesicle too close to the actin to permit binding of an additional myoVa. (*B*) With increasing intermotor distance (*I*), the motion of the vesicle becomes constrained, and the distance between the actin and vesicle (*d*) decreases. (*C*) Steric accessibility of binding sites (*Ac*), as a function of the coordinates position, relative to the vesicle ($X - X_{\text{vesicle}}$), and distance between motors (*I*). (*D*) We considered the potential impact of the specification of actin helical repeat in vesicle simulations. We consider three possibilities: "Strict" approximates the findings of Steffen et al. (1) in which for each 36-nm pseudorepeat of the actin helix, 18 nm are completely sterically inaccessible (blue line). "Relaxed" reproduces the 36-nm periodicity, but allows binding at all sites, with some more favorable than others (red line). "No Actin Repeat" ignores potential accessibility issues altogether (green line). (*E*) Resulting plots of binding-site accessibility for the strict and relaxed cases, which were then used to regulate binding in the vesicle motility simulation. (*F*) Actin geometry has little impact on the ultimate velocity of vesicle transport, except at very high motor density.

1. Steffen W, Smith D, Simmons R, Sleep J (2001) Mapping the actin filament with myosin. *Proc Natl Acad Sci USA* 98(26):14949–14954.

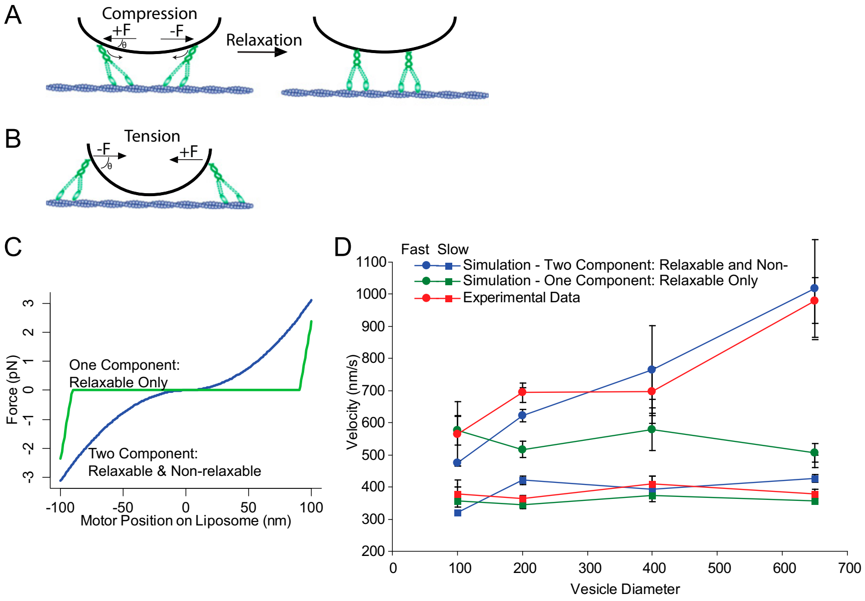

Fig. S8. Intermotor forces. (*A*) Compressive forces on the vesicle membrane and (*B*) tension on the vesicle membrane can be relaxed, but with larger motor separation distances, forces become more perpendicular to the vesicle membrane (θ ~ 90°), and cannot be fully relaxed, even with highly fluid (DOPC) membranes. Positive values of *F* indicate resistive forces—those directed opposite to myoVa's direction of motion, whereas negative values of *F* indicate forces in the assistive direction. (*C*) The contribution of the nonrelaxable term as a function of position, relative to the liposome (blue) defines the endpoint to which intermotor forces relax. The green curve illustrates a scenario in which all forces are considered to be relaxable (i.e., the nonrelaxable component is disregarded), except for situations where the motors are spaced as far apart as the vesicle's geometry will allow. (*D*) Using these two force definitions, DOPC vesicles of varying diameter were simulated. The velocity of the fast vesicle population is sensitive to the force profile, and only the complete, two-term force definition (blue) is able to reproduce the experimentally observed relationship between vesicle size and velocity (red).

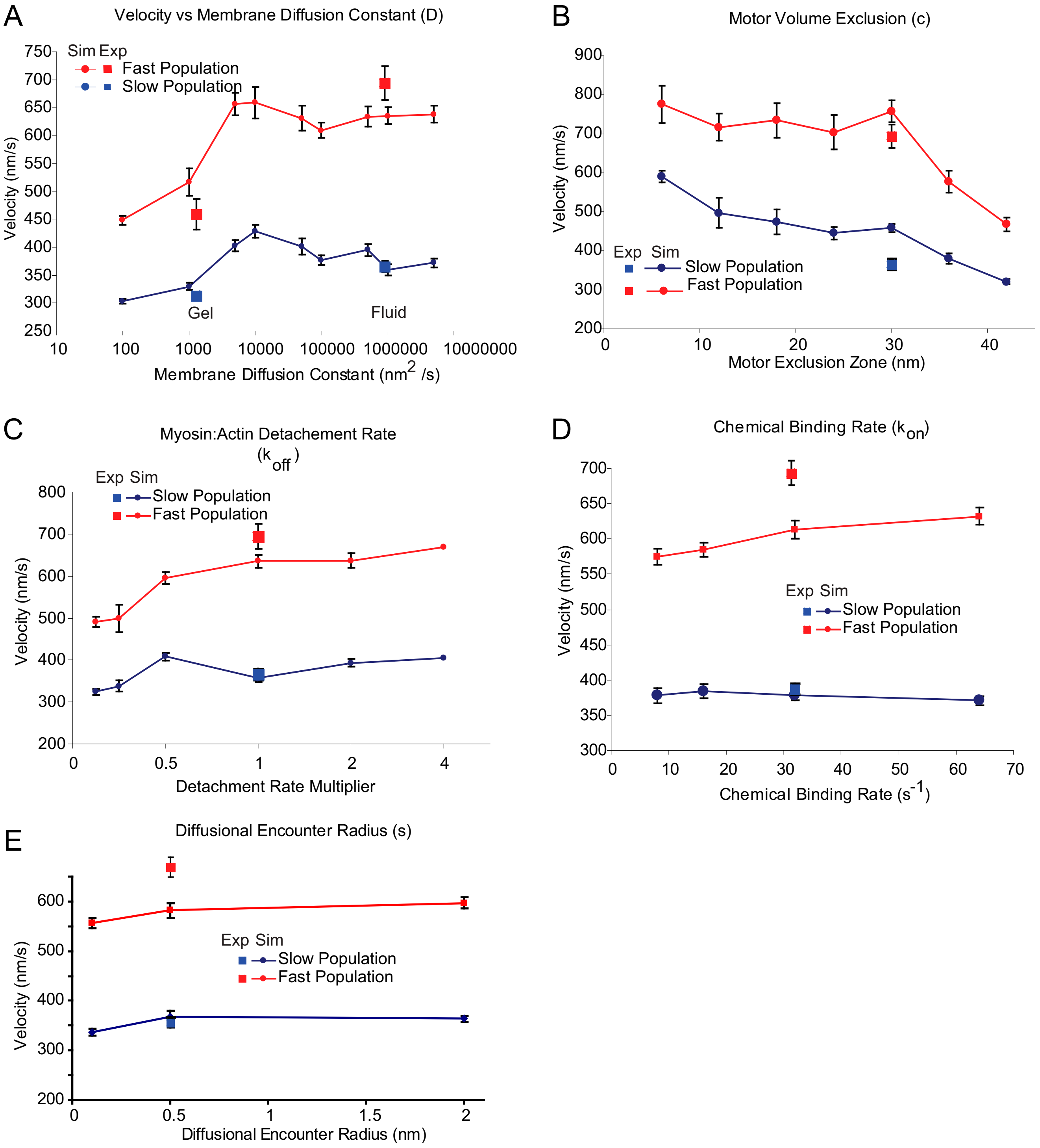

Fig. S9. Sensitivity analysis of model parameters. Response of the model for various parameters: (*A*) membrane diffusion constant, (*B*) motor volume exclusion (minimal distance between two actin-bound motor molecules), (*C*) load sensitivity of detachment, (*D*) "chemical" binding rate (rate of entry into strong binding state), and (*E*) diffusional encounter radius (distance at which an unbound myosin begins to interact with actin).

Table S1. Simulation rates and parameters

Parameter/rate	Symbol	Value	Citation
No. of motors per vesicle	N	4–64 per vesicle or 32–250 per μm^2	Refs. 1–3
Membrane diffusion constant	D	1,300 nm^2/s (DPPC); 9.1×10^5 nm^2/s (DOPC)	Ref. 4 and this study
Vesicle diameter	$2R$	100–650 nm	This study
MyoVa:actin chemical binding rate	k_{on}	32 s^{-1}	Ref. 5
MyoVa length	L	60 nm	Ref. 6
MyoVa bending stiffness	k	0.25 pN/nm	Refs. 7 and 8
Diffusional encounter radius	s	0.5 nm	Ref. 9
MyoVa step size	ΔX_{step}	36 ± 9 nm (mean ± SD)	Ref. 10
Motor volume exclusion	c	30 nm	This study (Fig. S8*B*)
Intermotor force	F	$\frac{k \cdot \Delta X_{\text{step}}}{N_{\text{bound}}} \cdot e^{\frac{-(t-t_{\text{step}})Dk}{k_B T}} + \frac{k \cdot (l/2)^2}{2(L+R)}$, where $l/2$ is the distance between motor and vesicle center and t_{step} is the time of last step or detachment (of any motor)	This study
MyoVa:actin binding rate	k_{bind}	$\frac{2\pi D k_{\text{on}}}{2\pi D + k_{\text{on}} \ln\left(\sqrt{\frac{4R^2}{N_{\text{free}}}}/s\right)}$	Ref. 9
MyoVa detachment rate	k_{off}	$0.1724 s^{-1} \cdot e^{-1.005 pN^{-1} \cdot F} + 0.2634 s^{-1}$	Fit to model in figure 13 in ref. 7
MyoVa step rate	k_{step}	$\left(\frac{e^{-\left(\frac{0.04\text{nm} \cdot F}{k_B T}\right)}}{13 s^{-1}} + \frac{e^{-\left(\frac{14\text{nm} \cdot F}{k_B T}\right)}}{426 s^{-1}}\right)^{-1}$	Ref. 10

1. Nascimento AA, Amaral RG, Bizario JC, Larson RE, Espreafico EM (1997) Subcellular localization of myosin-V in the B16 melanoma cells, a wild-type cell line for the dilute gene. *Mol Biol Cell* 8(10):1971–1988.
2. Tabb JS, Molyneaux BJ, Cohen DL, Kuznetsov SA, Langford GM (1998) Transport of ER vesicles on actin filaments in neurons by myosin V. *J Cell Sci* 111(Pt 21):3221–3234.
3. Gross SP, et al. (2002) Interactions and regulation of molecular motors in *Xenopus* melanophores. *J Cell Biol* 156(5):855–865.
4. Rubenstein JL, Smith BA, McConnell HM (1979) Lateral diffusion in binary mixtures of cholesterol and phosphatidylcholines. *Proc Natl Acad Sci USA* 76(1):15–18.
5. De La Cruz EM, Wells AL, Rosenfeld SS, Ostap EM, Sweeney HL (1999) The kinetic mechanism of myosin V. *Proc Natl Acad Sci USA* 96(24):13726–13731.
6. Liu J, Taylor DW, Krementsova EB, Trybus KM, Taylor KA (2006) Three-dimensional structure of the myosin V inhibited state by cryoelectron tomography. *Nature* 442(7099):208–211.
7. Vilfan A (2005) Elastic lever-arm model for myosin V. *Biophys J* 88(6):3792–3805.
8. Moore JR, Krementsova EB, Trybus KM, Warshaw DM (2004) Does the myosin V neck region act as a lever? *J Muscle Res Cell Motil* 25(1):29–35.
9. Lauffenburger DA, Linderman JJ (1993) *Receptors: Models for Binding, Trafficking, and Signaling* (Oxford Univ Press, New York).
10. Kad NM, Trybus KM, Warshaw DM (2008) Load and Pi control flux through the branched kinetic cycle of myosin V. *J Biol Chem* 283(25):17477–17484.